



**Self-Assembled Water-Soluble Nucleic Acid Probe
Tiles for Label-Free RNA Hybridization Assays**

Yonggang Ke, *et al.*
Science **319**, 180 (2008);
DOI: 10.1126/science.1150082

***The following resources related to this article are available online at
www.sciencemag.org (this information is current as of January 14, 2008):***

Updated information and services, including high-resolution figures, can be found in the online version of this article at:

<http://www.sciencemag.org/cgi/content/full/319/5860/180>

Supporting Online Material can be found at:

<http://www.sciencemag.org/cgi/content/full/319/5860/180/DC1>

This article **cites 14 articles**, 7 of which can be accessed for free:

<http://www.sciencemag.org/cgi/content/full/319/5860/180#otherarticles>

This article appears in the following **subject collections**:

Chemistry

<http://www.sciencemag.org/cgi/collection/chemistry>

Information about obtaining **reprints** of this article or about obtaining **permission to reproduce this article** in whole or in part can be found at:

<http://www.sciencemag.org/about/permissions.dtl>

reduce the form factor. Even without this indirect evidence for the predicted FFLO state, our main conclusion remains that in this strongly Pauli-limited superconductor with a quantum critical point at $H_{c2}(T=0)$, the mixed state departs in many respects from the classical Abrikosov VL.

References and Notes

- C. Petrović *et al.*, *J. Phys. Condens. Matter* **13**, L337 (2001).
- A. Bianchi, R. Movshovich, I. Vekhter, P. G. Pagliuso, J. L. Sarrao, *Phys. Rev. Lett.* **91**, 257001 (2003).
- M. A. Tanatar, J. Paglione, C. Petrović, L. Taillefer, *Science* **316**, 1320 (2007).
- A. M. Clogston, *Phys. Rev. Lett.* **9**, 266 (1962).
- A. Bianchi *et al.*, *Phys. Rev. Lett.* **89**, 137002 (2002).
- T. Tayama *et al.*, *Phys. Rev. B* **65**, 180504 (2002).
- R. Movshovich *et al.*, *Phys. Rev. Lett.* **86**, 5152 (2001).
- Y. Kasahara *et al.*, *Phys. Rev. B* **72**, 214515 (2005).
- A. A. Abrikosov, *Sov. Phys. JETP* **5**, 1174 (1957).
- A. I. Larkin, Y. N. Ovchinnikov, *Sov. Phys. JETP* **20**, 762 (1965).
- P. Fulde, R. A. Ferrell, *Phys. Rev. A* **550**, 135 (1964).
- Y. Matsuda, H. Shimahara, *J. Phys. Soc. Jpn.* **76**, 051005 (2007), and references therein.
- A. Bianchi, R. Movshovich, C. Capan, P. G. Pagliuso, J. L. Sarrao, *Phys. Rev. Lett.* **91**, 187004 (2003).
- X. Gratens *et al.*, <http://arxiv.org/abs/cond-mat/0608722> (2006).
- See supporting material on Science Online.
- M. R. Eskildsen, C. D. Dewhurst, B. W. Hoogenboom, C. Petrović, P. C. Canfield, *Phys. Rev. Lett.* **90**, 187001 (2003).
- L. DeBeer-Schmitt, C. D. Dewhurst, B. W. Hoogenboom, C. Petrović, M. R. Eskildsen, *Phys. Rev. Lett.* **97**, 127001 (2006).
- M. R. Eskildsen *et al.*, *Nature* **393**, 242 (1998).
- M. H. S. Amin, I. Affleck, M. Franz, *Phys. Rev. B* **58**, 5848 (1998).
- M. Ichioka, A. Hasegawa, K. Machida, *Phys. Rev. B* **59**, 8902 (1999).
- V. G. Kogan *et al.*, *Phys. Rev. B* **55**, R8693 (1997).
- S. P. Brown *et al.*, *Phys. Rev. Lett.* **92**, 067004 (2004).
- A. Vorontsov, I. Vekhter, *Phys. Rev. Lett.* **96**, 237001 (2006).
- N. Nakai, P. Miranović, M. Ichioka, K. Machida, *Phys. Rev. Lett.* **89**, 237004 (2002).
- A. Gurevich, V. G. Kogan, *Phys. Rev. Lett.* **87**, 177009 (2001).
- M. Franz, C. Kallin, P. I. Soininen, A. J. Berlinsky, A. L. Fetter, *Phys. Rev. B* **53**, 5795 (1996).
- R. J. Ormeno, A. Sibley, C. E. Gough, S. Sebastian, I. R. Fisher, *Phys. Rev. Lett.* **88**, 047005 (2002).
- S. Özcan *et al.*, *Europhys. Lett.* **62**, 412 (2003).
- J. Schelten, H. Ullmaier, W. Schmatz, *Phys. Status Solidi B* **48**, 619 (1971).
- J. R. Clem, *J. Low Temp. Phys.* **18**, 427 (1975).
- E. M. Forgan *et al.*, *Phys. Rev. Lett.* **88**, 167003 (2002).
- V. G. Kogan, N. V. Zhelezina, *Phys. Rev. B* **71**, 134505 (2005).
- J. E. Sonier, *J. Phys. Condens. Matter* **16**, S4499 (2004).
- L. DeBeer-Schmitt *et al.*, *Phys. Rev. Lett.* **99**, 167001 (2007).
- M. Ichioka, K. Machida, *Phys. Rev. B* **76**, 064502 (2007).
- R. Settai *et al.*, *J. Phys. Condens. Matter* **13**, L627 (2001).
- This work is based on experiments performed at the Swiss spallation neutron source SINQ, Paul Scherrer Institute, Villigen, Switzerland. Supported by NSF grant NSF-DMR-0600742 (A.D.B. and Z.F.), the Alfred P. Sloan Foundation (M.R.E.), the European Commission under the 6th Framework Programme through the Key Action: Strengthening the European Research Area, Research Infrastructures (contract RII3-CT-2003-505925), the Swiss National Science Foundation (contract PP002-102831), the Swiss National Center of Competence in Research program "Materials with Novel Electronic Properties," the UK Engineering and Physical Sciences Research Council, and the U.S. Department of Energy, Office of Basic Energy Sciences. Part of this work was carried out at the Brookhaven National Laboratory, which is operated for the U.S. Department of Energy by Brookhaven Science Associates (DE-Ac02-98CH10886). We thank L. N. Bulaeviskii, C. Capan, V. G. Kogan, K. Machida, and I. Vekhter for discussions during the preparation of the manuscript.

Supporting Online Material

www.sciencemag.org/cgi/content/full/319/5860/177/DC1

Materials and Methods

Fig. S1

17 September 2007; accepted 21 November 2007

10.1126/science.1150600

Self-Assembled Water-Soluble Nucleic Acid Probe Tiles for Label-Free RNA Hybridization Assays

Yonggang Ke,^{1,3} Stuart Lindsay,^{1,3,4} Yung Chang,^{2,5} Yan Liu,^{1,3} Hao Yan^{1,3,*}

The DNA origami method, in which long, single-stranded DNA segments are folded into shapes by short staple segments, was used to create nucleic acid probe tiles that are molecular analogs of macroscopic DNA chips. One hundred trillion probe tiles were fabricated in one step and bear pairs of 20-nucleotide-long single-stranded DNA segments that act as probe sequences. These tiles can hybridize to their targets in solution and, after adsorption onto mica surfaces, can be examined by atomic force microscopy in order to quantify binding events, because the probe segments greatly increase in stiffness upon hybridization. The nucleic acid probe tiles have been used to study position-dependent hybridization on the nanoscale and have also been used for label-free detection of RNA.

The detection of low levels of gene expression (*I*) has been enabled by technologies such as DNA microarrays (2, 3) and reverse transcription polymerase chain reaction (RT-PCR) (4). Nonetheless, these technologies are still expensive (5), require probe labeling, and are hard to scale down to sample volumes comparable to those of single cells.

Sample volumes have been reduced and sensitivities have been increased, but target detection still relies heavily on enzymatic manipulation and amplification to create detectable signals. We present an alternative that complements benchtop arrays in which individual self-assembled nucleic acid "tile" molecules, formed by "stapling" long, single-stranded DNA segments with shorter strands into shapes, can act as hybridization probes for molecules such as mRNAs in solution. After binding, the tiles can be adsorbed onto mica surfaces and are detected by atomic force microscopy (AFM). Thus, the probe tiles are reagents that are hybridized in solution and then titrated to quantify the targets.

Because the probes are placed on each nucleic acid tile with nanometer-scale precision, the effects of probe placement can be explored with

molecular resolution. We found that the exact position of the probe made a substantial difference to hybridization efficiency. We circumvented this problem by manufacturing "bar-coded" tiles in which all of the probes were placed in an optimal position, and each type of nucleic acid tile was distinguished with a distinctive code represented by a group of dumbbell-shaped DNA loops protruding out of the tile surface as topographic registration markers; each coded tile detected one gene product.

Our ability to detect single-molecule hybridization with AFM appears to be enabled by the difference in the elastic properties of single- and double-stranded DNA or of the RNA-DNA hybrid. Detection sensitivity was, in this case, limited only by nucleic acid tile concentration down to the 200 pM levels, which we were able to image readily.

The design of the nucleic acid probe tiles and the read-out mechanism for the target binding are illustrated in Fig. 1. The foundation of the tile design was based on "scaffolded DNA origami" (Fig. 1A): a self-assembling technique for one-step synthesis of fully addressable DNA nanostructures (6). Rothmund (6) demonstrated that a long, single-stranded viral DNA scaffold can be folded and stapled by a large number of short synthetic "helper strands" into nanostructures that display complex patterns. A one-step nanomolar-scale synthesis yields $>10^{14}$ origami tiles with nearly 100% yield.

We used a simple, rectangular-shaped design, and its layout is shown schematically in Fig. 1A. Three different sequences of capture probes were included on the origami tile, corresponding to a region of three genes—*Rag-I*, *c-myc*,

¹Center for Single Molecule Biophysics, Arizona State University, Tempe, AZ 85287, USA. ²Center for Infectious Diseases and Vaccinology, The Biodesign Institute, Arizona State University, Tempe, AZ 85287, USA. ³Department of Chemistry and Biochemistry, Arizona State University, Tempe, AZ 85287, USA. ⁴Department of Physics, Arizona State University, Tempe, AZ 85287, USA. ⁵School of Life Sciences, Arizona State University, Tempe, AZ 85287, USA.

*To whom correspondence should be addressed. E-mail: hao.yan@asu.edu

and β -actin—expressed in the murine progenitor B cell line (7, 8). A sequence not found in the mouse genome was added as a control. Twelve copies of each probe were arranged into each line on the tile, with an interprobe distance within the lines of 5 nm and a spacing between the lines of 20 nm (Fig. 1A). Six copies of the control probes form a shorter line on the left side of the tile. An “index spot” was placed in the top left corner. We used six of the 28-nucleotide-long dumbbell-shaped structures [described elsewhere (6)] as “permanent” features to break the symmetry of the tile, so that the images of the tiles could be oriented unambiguously. Detailed sequences of the probes, control, and indexes can be found in the supporting online material (9).

The tiles were self-assembled in solution: We used the single-stranded M13 viral genome scaffold

strand to nucleate both the probe-modified and nonmodified helper strands. An aliquot of the solution (2 μ l) was dropped onto the mica surface for AFM imaging (Fig. 1B). In our probe design, selected pairs of neighboring helper strands are modified so that each contains a single-stranded fragment of 20 nucleotides that protrudes out of the tile surface (Fig. 1C). Each dangling single strand in the pair serves as a half-probe for a single RNA target of 40 bases. Upon hybridization of the target to a pair of half-probes, the strands form a stiff V-shaped structure [see (9) for molecular dynamics simulation]. This local stiffening is readily sensed mechanically with an AFM cantilever and appears in the image as local high-spot (Fig. 1C). We have tried various different probe designs (9), and this V-shaped junction design provides the best AFM signal of target binding.

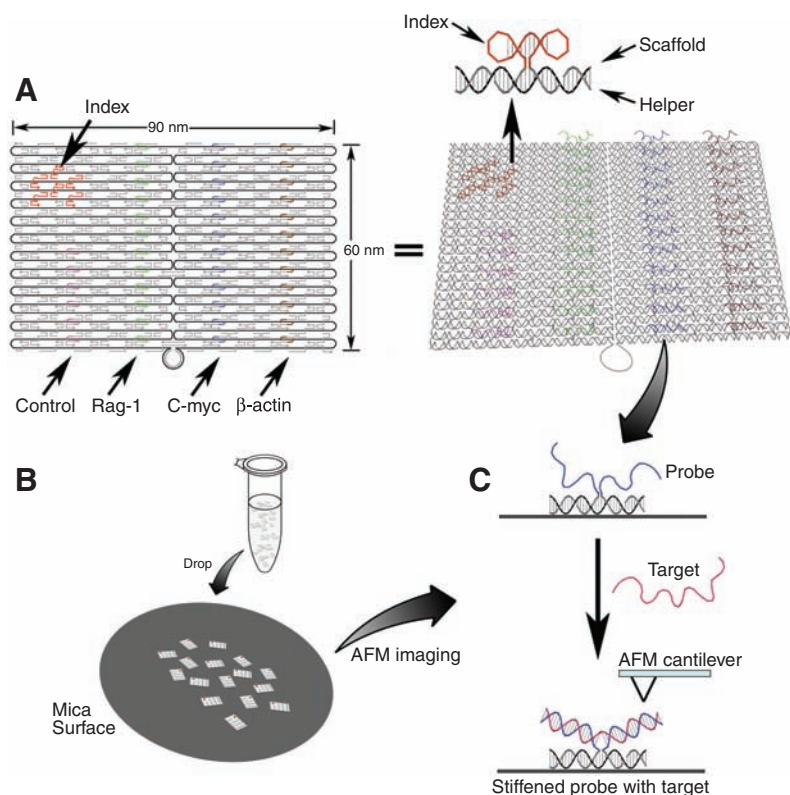


Fig. 1. (A) (Left) Schematic layout of the indexed nucleic acid probe tiles bearing three different probes (for targets *Rag-1*, *C-myc*, and β -actin) and a control probe. A simple, rectangular-shaped DNA origami tile was used, in which a circular single-stranded M13 viral DNA (black lines), composed of 7249 bases, is folded and stapled, with the help of >200 short synthetic DNA strands, to form the desired two-dimensional (2D) tile. Helper strands without probe modifications are shown (gray lines), and helper strands modified with probe sequences and control sequences are shown in different colors. This rectangular-shaped probe tile has dimensions of 90 nm by 60 nm. Twelve copies of the specific probes are spaced at 5-nm intervals in a line, and lines of probes are separated by 20 nm. Six control probes are arranged in a shorter line. An index spot, composed of six closely packed dumbbell-shaped bulge loops at the top left corner, is designed to give the AFM topological feature with which to orient the AFM image of each individual tile. (Right) Tilted view of the tile (drawn in DNA helix style) to illustrate the 3D view of the probe tile layout. (B) Illustration of the process (not drawn to scale) for the use of probe tiles for target detection. Probe tiles are self-assembled in solution, hybridized with targets, and then dropped onto the mica surface for AFM imaging. (C) Probe design and detection mechanism. A pair of neighboring helper strands is extended out of the surface of the tile, with each 20-base-long extension bearing a half of the target sequence. These single-stranded probes are flexible and do not produce a visible feature under AFM imaging. Upon target hybridization with the pair of half-probes, the double helix of the DNA-RNA duplex forms, and the stiffer V-shaped junction is readily detected with the AFM cantilever.

In a test of the initial design, tiles with all three probes and a control (Fig. 1A) were assembled with 10 nM of the M13 viral genome as the scaffold strand and a fivefold excess of short helper strands. Because the existence of the excess helper strands (some of which contain the probe sequences) will interfere with the target hybridization, the tiles were purified with Microcon centrifugal filter devices [MWCO 100,000 (Millipore, Bedford, MA)] to remove the small oligonucleotides. We adjusted the final concentration of the tile by using optical absorption at 260 nm. We then mixed 10 nM of the tiles with 600 nM {a [probe]/[target] ratio of 1:5} of each of the three different targets. AFM images of these hybridized tiles revealed that the target hybridization depends strongly on the probe positions in the tile. The probes on the edge (β -actin at position 3) give the best hybridization efficiency, whereas the probes in the middle of the tile (*Rag-1* at position 1) give the worst binding efficiency (fig. S5).

To confirm that this positional effect does not depend on the sequence of the probes, we put the same probes with the worst binding (*Rag-1*) at all three positions and found again that the probes on the edge (position 3) gave the best hybridization efficiency (Fig. 2 and fig. S6). Because electric-charge repulsions between the target and the underlying tile, as well as repulsions between probes, are stronger in the middle of the tile than at the edge of the tile, and because steric hindrance is weakest at the tile's edge, these factors presumably play a role in our observed results. In the DNA microarray, interprobe spacing is not controlled at the single-molecule level. Hybridization on a solid surface is not only kinetically slow but also less efficient (10, 11). Our probe tile design now permits the study of the positional effect of probes on their efficiency of target binding. The precise interprobe-distance control and the hybridization in solution also make the binding kinetically fast, with full hybridization within 30 min with no stirring at room temperature.

The self-assembling nucleic acid tile (12–14) allows accurate control of probe placement (15, 16). We designed four different bar-coded tiles (Fig. 3A), each of which carried a line of probes: one for each of the three targets and one as a control. The probes were placed along one edge of the tiles to optimize the hybridization efficiency, and a bar-coded region was added, in which combinations of different index geometries were used to distinguish the tile. An equimolar mix of the four types of tiles was used for simultaneous multiplex detection. Typical AFM images (Fig. 3A, middle panel) show that each bar-coded tile can be distinguished by its own bar code, without targets.

We used these bar-coded probe tiles to test the detection of single and multiple targets (Fig. 3, A and B, and fig. S9). The detection of the three different targets is highly specific, with no binding of the control sequence. Each probe also serves as a control for the other two probes and revealed no nonspecific cross-hybridization. To

demonstrate that our system can detect a synthetic RNA target in the presence of a large amount of cellular RNA, we performed a spike experiment in our hybridization by mixing the synthetic RNA with 2 mg/ml total cellular RNA. The target hybridization can still be visualized (Fig. 3B, right panel), and the excess amount of cellular RNA did not interfere with the specific target hybridization. The use of the tile probes for RNA detection is also sensitive to the amount of

targets added. Figure 3C shows the obvious difference of the hybridization efficiency between low and high target concentrations.

Because the nucleic acid probe tiles are themselves reagents, it is possible to titrate the probes against the targets and obtain quantitative results, as shown in Fig. 4 for two different tile concentrations (10 nM and 200 pM). The plots of hybridization efficiency versus $[\text{target}]/[\text{probe}]$ ratios at these two tile concentrations show a similar trend:

a nearly linear increase at $[\text{target}]/[\text{probe}] < 1$ that reaches saturation at $[\text{target}]/[\text{probe}] > 1$. This non-Michaelis-Menten (i.e., linear) binding shows that the detection is limited only by the concentration of the tiles; every target molecule is bound by a probe at these concentrations. This result is expected, given that the hybridization free energy is about -50 kcal/mol (17), and it is a clear indication that the intrinsic hybridization efficiency is 100% and that the kinetics are not limiting.

Our current sensitivity is limited by our use of large substrates for AFM imaging and by conventional micropipette handling of reagents. To improve the detection for profiling gene expression of single cells, we propose that further developments are needed to deposit a smaller amount of tiles onto a tiny spot for AFM imaging. For example, if tiles as small as 1 nl of 1 pM solution (the tiles are dilutable) could be placed on an optically indexed AFM stage for imaging, it would bring the detection limit down to ~ 1000 molecules, which would be adequate for label-free and PCR-free detection of the product of gene expression in a single cell. Although this approach does not yet compete with existing arrays for analysis with hundreds of thousands of probes, it can probe the effects of nanometer-scale changes in geometry, as demonstrated by our measurements of the position dependence of hybridization. Such investigations need not be limited to DNA or RNA analysis. For example, we have shown that proteins can be placed onto these tiles with nanometer-scale precision using DNA aptamers (18). Thus,

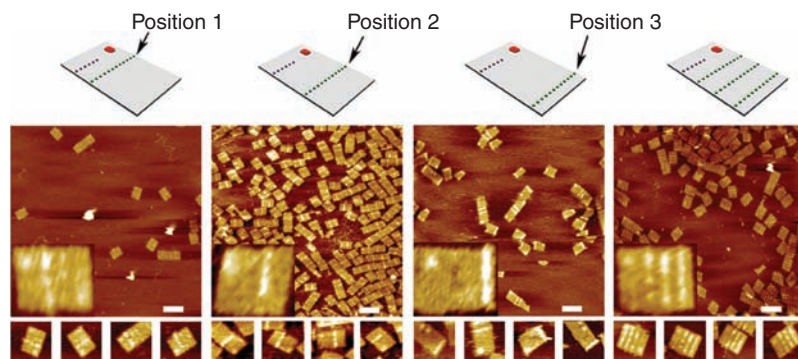


Fig. 2. The effect of the probe positions on the efficiency of target binding. The three lines (positions 1 to 3) are all composed of the same probes for *Rag-1*. Four different DNA tiles are constructed: three tiles with probes at one of the three positions, and one tile with the same probes at all three positions. The target-binding efficiency is measured by analyzing the height images by AFM (9). Topographic illustrations of the tile design and their corresponding AFM images with a $[\text{target}]/[\text{probe}]$ ratio of 5:1 in all cases are shown. Scale bars, 150 nm. Four representative zoom-in images are shown in the bottom-left corner of each large-area scan. An enlarged zoom-in image is also shown in the bottom-left corner of the large-area scan. Additional enlarged images and a plot of hybridization percentage versus probe positions can be found in (9).

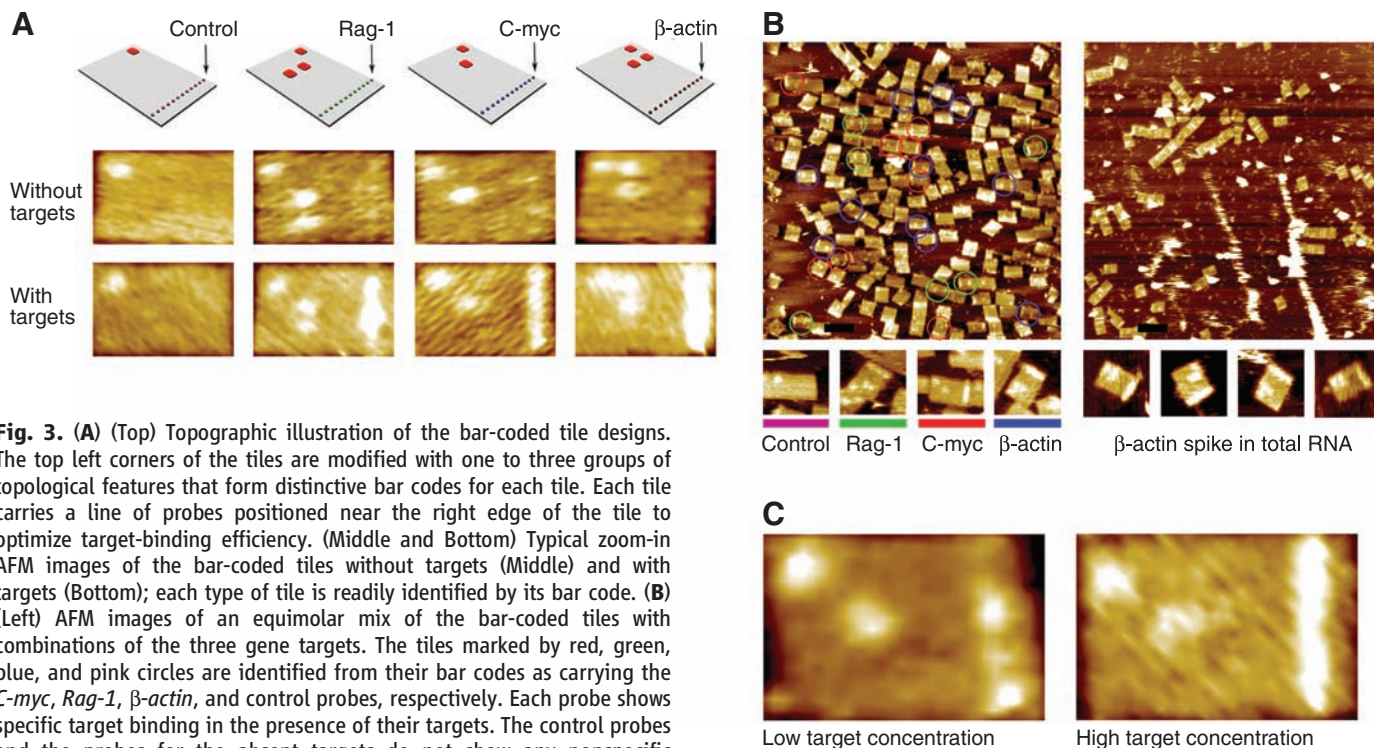


Fig. 3. (A) (Top) Topographic illustration of the bar-coded tile designs. The top left corners of the tiles are modified with one to three groups of topological features that form distinctive bar codes for each tile. Each tile carries a line of probes positioned near the right edge of the tile to optimize target-binding efficiency. (Middle and Bottom) Typical zoom-in AFM images of the bar-coded tiles without targets (Middle) and with targets (Bottom); each type of tile is readily identified by its bar code. (B) (Left) AFM images of an equimolar mix of the bar-coded tiles with combinations of the three gene targets. The tiles marked by red, green, blue, and pink circles are identified from their bar codes as carrying the *C-myc*, *Rag-1*, β -actin, and control probes, respectively. Each probe shows specific target binding in the presence of their targets. The control probes and the probes for the absent targets do not show any nonspecific binding. (Right) β -actin RNA spike experiment in the presence of 2 mg/ml cellular total RNA extract. The detection efficiency of the β -actin target is not interfered by the presence of a high concentration of the cellular RNA. Scale bars, 150 nm. (C) Typical AFM images showing the sensitivity

of the probe tile to target concentration (with the *C-myc* target as an example). The $[\text{target}]/[\text{probe}]$ ratios of 0.2:1 (left) and 2:1 (right) are shown. Dimensions of each tile in all images were measured to be ~ 60 nm by 90 nm.

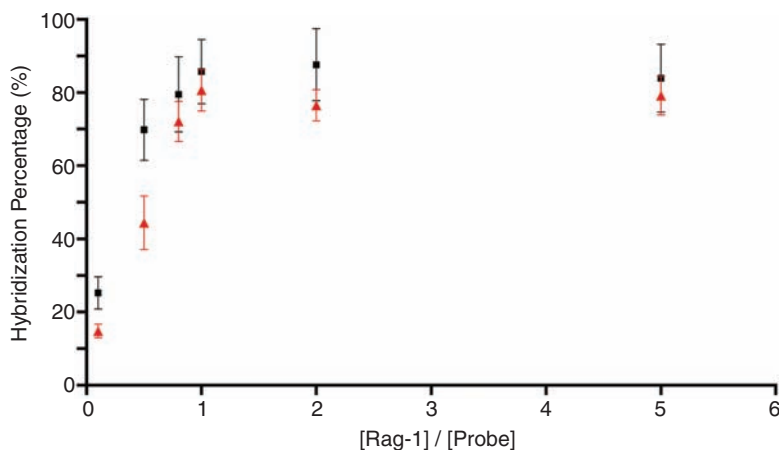


Fig. 4. Hybridization percentage as a function of the [target]/[probe] ratio. The tile used is the one shown in Fig. 3A carrying the *Rag-1* probes. Two different tile concentrations are used: 10 nM (black squares) and 200 pM (red triangles). Each error bar represents SD calculated from measurements on 50 tiles.

it should be possible to probe the spatial dependence of binding interactions involving multiple biomolecular components.

References and Notes

- D. R. Meldrum, *Science* **292**, 515 (2001).
- U. R. Mueller, D. V. Nicolau, *Microarray Technology and its Applications* (Springer-Verlag, Berlin, 2004).
- M. Schena, D. Shalon, R. W. Davis, P. O. Brown, *Science* **270**, 467 (1995).
- S. A. Bustin, T. Nolan, in *Real-Time PCR: An Essential Guide*, K. Edwards, J. Logan, N. Saunders, Eds. (Horizon Bioscience, Norfolk, UK, 2004).
- Y. H. Yang, T. Speed, *Nat. Rev. Genet.* **3**, 579 (2002).
- P. W. K. Rothmund, *Nature* **440**, 297 (2006).
- Y. Chang, M. L. Brown, *Proc. Natl. Acad. Sci. U.S.A.* **96**, 191 (1999).

- E. A. Jacobsen, O. Ananieva, M. L. Brown, Y. Chang, *J. Immunol.* **176**, 6831 (2006).
- See supporting material on Science Online.
- A. W. Peterson, R. J. Heaton, R. M. Georgiadis, *Nucleic Acids Res.* **29**, 5163 (2001).
- Y. Gao, L. K. Wolf, R. M. Georgiadis, *Nucleic Acids Res.* **34**, 3370 (2006).
- N. C. Seeman, *Nature* **421**, 427 (2003).
- E. Winfree, F. Liu, L. A. Wenzler, N. C. Seeman, *Nature* **394**, 539 (1998).
- H. Yan, S. H. Park, G. Finkelstein, J. H. Reif, T. H. LaBean, *Science* **301**, 1882 (2003).
- K. Lund, Y. Liu, S. Lindsay, H. Yan, *J. Am. Chem. Soc.* **127**, 17606 (2005).
- S. H. Park *et al.*, *Angew. Chem. Int. Ed.* **45**, 735 (2006).
- M. Zuker, D. H. Mathews, D. H. Turner, in *RNA Biochemistry and Biotechnology*, J. Barciszewski, B. F. C. Clark, Eds. (Kluwer Academic, Dordrecht, Netherlands, 1999), pp. 11–43.
- R. Chhabra *et al.*, *J. Am. Chem. Soc.* **129**, 10304 (2007).
- This research is partly supported by funding from NIH (to S.L. and H.Y.) and from NSF, Office of Naval Research, and U.S. Air Force Office of Scientific Research (to H.Y.).

Supporting Online Material

www.sciencemag.org/cgi/content/full/319/5860/180/DC1
Materials and Methods
Sequence Information
Figs. S1 to S16

4 September 2007; accepted 21 November 2007
10.1126/science.1150082

Imaging Nucleophilic Substitution Dynamics

J. Mikosch,¹ S. Trippel,¹ C. Eichhorn,¹ R. Otto,¹ U. Lourderaj,²
J. X. Zhang,² W. L. Hase,² M. Weidemüller,¹ R. Wester^{1*}

Anion-molecule nucleophilic substitution (S_N2) reactions are known for their rich reaction dynamics, caused by a complex potential energy surface with a submerged barrier and by weak coupling of the relevant rotational-vibrational quantum states. The dynamics of the S_N2 reaction of $\text{Cl}^- + \text{CH}_3\text{I}$ were uncovered in detail by using crossed molecular beam imaging. As a function of the collision energy, the transition from a complex-mediated reaction mechanism to direct backward scattering of the I^- product was observed experimentally. Chemical dynamics calculations were performed that explain the observed energy transfer and reveal an indirect roundabout reaction mechanism involving CH_3 rotation.

Bimolecular nucleophilic substitution is a fundamental reaction mechanism in chemistry (1). The reaction's equation, $\text{X} + \text{R-Y} \rightarrow \text{X-R} + \text{Y}$, summarizes bond formation by the attacking nucleophile X with the moiety R and concerted bond cleavage of the substituted leaving group Y. S_N2 reactions are widely used in preparative organic synthesis (2). Low-energy negative-ion reactions, most likely nucleophilic substitution, are suggested

to cause the large amount of DNA double strand breaks in the wake of ionizing particles (3).

Anion-molecule S_N2 reactions may be the most prominent type of ion-molecule reactions, studied extensively both experimentally (4, 5) and computationally (6, 7). Rate coefficients for these reactions depend strongly on the surrounding solvent (4), making experiments on isolated gas-phase systems a crucial reference point in distinguishing solvent effects from the intrinsic dynamics of the reaction. The low rate coefficients observed in the gas phase, which are much smaller than the classical Langevin capture rate expected for a barrier-less ion-molecule reaction, are qualitatively well understood to stem from two wells (Fig. 1) on the potential energy hypersurface (8).

This characteristic potential energy landscape is attributed to the formation of ion-dipole collision complexes on both sides of the reaction barrier. The barrier itself, which represents a transition state that corresponds to inversion at the reaction center, has a substantial influence on the reaction kinetics even though it most often lies submerged with respect to the energy of the reactants.

Studies of anion-molecule S_N2 reactions have determined reaction rates as a function of temperature (9, 10) and energy (11) and probed the dynamics of the pre- and postreaction ion-dipole complexes (12, 13). An important finding from these studies is that the reaction kinetics and dynamics are often inadequately described by statistical theories (14–16, 12, 17), a result supported by classical (6, 18) and quantum (19, 7, 20) chemical dynamics simulations. An illustrative example of nonstatistical behavior is the strong dependence of the $\text{Cl}^- + \text{CH}_3\text{Br}$ reaction rate on the relative translational energy of the reactants, despite insensitivity to their internal temperature (14). Such dynamics contradict the statistical assumption of rapid randomization of all the available energy in the $\text{Cl}^- \cdot \text{CH}_3\text{Br}$ prereaction complex. Nonstatistical dynamics of the ion-dipole complexes are also evident in the product energy partitioning for the $\text{Cl}^- \cdot \text{CH}_3\text{I}$ unimolecular decomposition (13), the mode-specific dynamics of the $\text{Cl}^- \cdot \text{CH}_3\text{Br}$ complex (12, 21), and the $\text{Cl}^- + \text{CH}_3\text{Br}$ reaction rate dependence on collision energy (11). Therefore, a detailed analysis of the flow of energy during the course of the reaction is required (6).

¹Physikalisches Institut, Universität Freiburg, Hermann-Herder-Straße 3, 79104 Freiburg, Germany. ²Department of Chemistry and Biochemistry, Texas Tech University (TTU), Lubbock, TX 79409, USA.

*To whom correspondence should be addressed. E-mail: roland.wester@physik.uni-freiburg.de